We are IntechOpen, the world's leading publisher of Open Access books Built by scientists, for scientists

4,800
Open access books available

122,000
International authors and editors

135M
Downloads

Our authors are among the

154
Countries delivered to

TOP 1%
most cited scientists

12.2%
Contributors from top 500 universities

WEB OF SCIENCE™

Selection of our books indexed in the Book Citation Index in Web of Science™ Core Collection (BKCI)

Interested in publishing with us?
Contact book.department@intechopen.com

Numbers displayed above are based on latest data collected.
For more information visit www.intechopen.com

Chapter 3

Coupled Model of Precipitates and Microsegregation During Solidification

Yandong Li, Huamei Duan and Cheng Peng

Additional information is available at the end of the chapter

http://dx.doi.org/10.5772/intechopen.72597

Abstract

To understand the precipitation behavior and solidification process of micro-alloyed steel, abundant thermodynamic data of pure substances were incorporated in the coupled thermodynamic model of inclusions precipitation and solutes micro-segregation during the solidification of heat-resistant steel containing cerium. The liquid inclusions $Ce_{2x}Al_{2y}Si_{1-x-y}O_z$ where $0 < x < 1$, $0 < y < 1-x$ and $z = 1-x-y$ and their generation Gibbs free energy were first introduced to the inclusions reactions according to the Al_2O_3-SiO_2-Ce_2O_3 phase diagram. Then plant trials, lab experiments and published work in the literature were taken account to valid the established model. Also, the difference of calculated results between FactSage and this model were argued. Finally, the liquid inclusions were found in the samples from experiments in the tube furnace based on the calculations by this model.

Keywords: liquid inclusions, thermodynamic model, rare earth, heat-resistant steel

1. Introduction

The heat resistant steels containing rare earth elements (RE) have absolute advantages in mechanical properties and corrosion resistance [1–4]. The oxidation resistance of 253MA steel at high temperature is dramatically enhanced as alloyed with cerium element. However, the rare earth elements are used as deoxidizing and desulfurizing agents in the earlier ages owing to the strong oxidation property [5]. As a result, a large number of inclusions such as Ce_2O_3 and Ce_2O_2S with high melting temperature and small size are generated in the molten steel. During the continuous casting process these inclusions are easily captured by the submerged nozzle. Then the accumulated inclusions with frozen steel lead to nozzle blocking and the production process is interrupted [6–9]. As one of the effectual solutions to nozzle blocking calcium treatment can modify the solid alumina clusters to liquid inclusions which have weak affinity force with the nozzle inner wall [10–13]. Inspired by the above method, the high

melting point inclusions containing rare earth elements may be modified to liquid phase by some alloys to solve the nozzle clogging issue of heat resistant steel.

Many prediction models of inclusions formation and evolution are reported in the previous reports. However, the released self-built model mainly involve a few equilibrium reactions of alloy elements with oxygen or sulfur at 1600°C [14, 15]. And the thermodynamic properties of complex liquid inclusions, such as Mn-Si-Al-O, Ca-Al-O, Ca-Al-Mg-O, are calculated by the commercial software [15–19]. Harada assessed the $CaO\text{-}Al_2O_3$ liquid inclusions formation setting the fixed ratio of CaO to Al_2O_3 instead of the whole liquid region [20, 21]. FactSage as the common software in metallurgical field is strong at the equilibrium calculations of multi phases, but the FToxide database is short of solution thermodynamic data containing rare earth and the solidification model is not thoroughly optimized. Liu released one coupling model of micro-segregation and inclusion formation during solidification process in silicon steels [22]. However, the number of reactions was restricted and the solution phase was not considered. Fang proposed a thermodynamic model which includes plenty of formation reactions of rare earth inclusions except the liquid inclusions as a pity [23]. To make up for the deficiency of previous models [24], the more ampler generation reactions of inclusions especially the liquid phase coupling with the solute micro-segregation are introduced in the present model. Then the coupled model was validated by various methods, such as plant trials, lab scale experiments and released experimental data. Finally, the formation regions of liquid phases in the predominance diagrams were given. Moreover, the liquid inclusions with sphere shape and large size were found in the exploitative experiments of lab scale.

2. Modeling process

The coupling model is composed of two parts: the thermodynamic model of inclusions precipitation both in liquid and solid and the dynamic model of solute micro-segregation model in the liquid–solid interface during solidification. The schematic diagram of coupling process is shown in **Figure 1**. Considering the kinetic factors such as diffusion rate and atomic size, the inclusions with large size are formed in the residual liquid phase above the solidus temperature and the small-size carbonitrides are precipitated in the solidified steel under the liquidus temperature. All the relevant reactions of inclusions generation both in liquid and solidified steel are listed in **Table 1** [26–33] and **Table 2** [34–37], respectively. The activity standard state of solute elements and inclusions was 1 mass% infinite dilute solution and the pure substance, respectively. The activity coefficients of solute elements were arranged by Wagner's relations expanded to second order interaction coefficient. The solute segregation at liquid–solid interface during solidification was calculated form the Brody-Flemings micro-segregation model modified by Clyne-Kurz [25]. The more details including the mathematic expressions and thermodynamic properties of solutes can be consulted from the previous works [24].

The generated liquid inclusions whose activity is 1 can be identified as one isolated phase (pure liquid phase) out of the solid inclusions (pure solid phase) and solute elements (solutes in the infinite dilute solution) in the system. As the same as listed in **Table 1**, the liquid inclusion in the form of $Ce_{2x}Al_{2y}Si_{1\_x\_y}O_z$ (l, $0 < x < 1$, $0 < y < 1\_x$ and $z = 1\_x\_y$) is introduced

http://dx.doi.org/10.5772/intechopen.72597

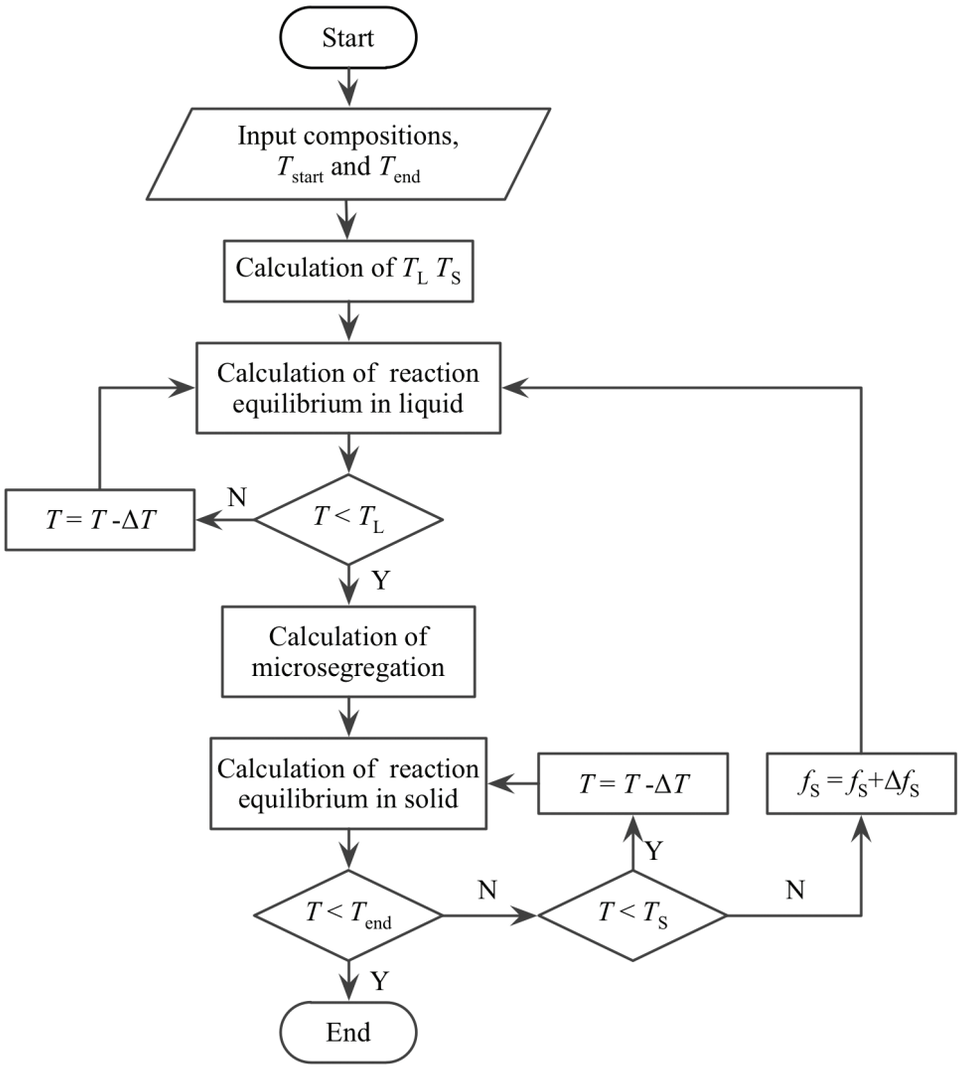

Figure 1. The simplified diagram of coupling process (fs—solid fraction).

according to the phase diagram of Al_2O_3-SiO_2-Ce_2O_3 system. The hard task is the calculation of standard Gibbs free energy of $Ce_{2x}Al_{2y}Si_{1-x-y}O_z$ generation as the following reaction:

$$x[\mathrm{Ce}] + 2y[\mathrm{Al}] + (1-x-y)[\mathrm{Si}] + z[\mathrm{O}] = \mathrm{Ce}_{2x}\mathrm{Al}_{2y}\mathrm{Si}_{1-x-y}\mathrm{O}_z(l) \tag{1}$$

The chemical reaction of Eq. 1 can be derived from the following reactions:

$$2[\mathrm{Ce}] + 3[\mathrm{O}] = \mathrm{Ce_2O_3}(s) \tag{2}$$

$$2[\mathrm{Al}] + 3[\mathrm{O}] = \mathrm{Al_2O_3}(s) \tag{3}$$

$$[\mathrm{Si}] + 2[\mathrm{O}] = \mathrm{SiO_2}(s) \tag{4}$$

$$\mathrm{Ce_2O_3}(s) = \mathrm{Ce_2O_3}(l) \quad \Delta G^{\theta} = 63086.4 - 25.1T \quad J \cdot mol^{-1} \tag{5}$$

$$\mathrm{Al_2O_3}(s) = \mathrm{Al_2O_3}(l) \quad \Delta G^{\theta} = 110756.7 - 46.8T \quad J \cdot mol^{-1} \tag{6}$$

Reaction equations in molten steel	$\Delta G^{\theta} = A + B \times T$, J·mol^{-1}	
	A	*B*
2[Ce] + 3[O] = Ce_2O_3(s)	−1,431,090	360.06
[Ce] + 2[O] = CeO_2(s)	−854274.7	249.11
[Ce] + [S] = CeS(s)	−422,783	120.58
[Ce] + 2[S] = CeS_2(s)	−131,000	121.4
2[Ce] + 3[S] = Ce_2S_3(s)	−1,074,584	328.24
3[Ce] + 4[S] = Ce_3S_4(s)	−1,493,010	438.9
2[Ce] + 2[O] + [S] = Ce_2O_2S(s)	−1353592.4	331.6
[Ce] + [Al] + 3[O] = $CeAlO_3$(s)	−1,366,460	364
[Ce] + 11[Al] + 3[O] = $CeAl_{11}O_{18}$(s)	−7261120.00	2282.36
2[Ce] + [Si] + 5[O] = Ce_2SiO_5(s)	−2077830.00	632.57
4.67[Ce] + 3[Si] + 13[O] = $Ce_{4.67}Si_3O_{13}$(s)	−5299450.00	1641.95
2[Ce] + 2[Si] + 7[O] = $Ce_2Si_2O_7$(s)	−2800700.00	909.66
$2x$[Ce] + $2y$[Al] + (1-x-y)[Si] + z[O] = $Ce_{2x}Al_{2y}Si_{1-x-y}O_z$(l)	—	—
[Ce] + [N] = CeN(s)	−401,200	153
[Ce] + 2[C] = CeC_2(s)	−202,790	125.3
2[Ce] + 3[C] = Ce_2C_3(s)	−224,000	205.8
[Al] + [N] = AlN(s)	−267,520	119.54
2[Al] + 3[O] = Al_2O_3(s)	−1,205,090	387.72
[Mn] + [S] = MnS(s)	−172676.1	56.07
[Mn] + [O] = MnO(s)	−284,420	122.75
[Si] + 2[O] = SiO_2(s)	−580,550	221.03
6[Al] + 2[Si] + 13[O] = $Al_6Si_2O_{13}$(s)	−4,758,434	1579.22
4[Cr] + [C] = Cr_4C(s)	−195,790	218
23[Cr] + 6[C] = $Cr_{23}C_6$(s)	−887889.7	1253.96
7[Cr] + 3[C] = Cr_7C_3(s)	−356120.1	417.62
3[Cr] + 2[C] = Cr_3C_2(s)	−182030.1	207.39
2[Cr] + 3[O] = Cr_2O_3(s)	−797,190	349.72
3[Cr] + 4[O] = Cr_3O_4(s)	−94439.9	416.79
[Cr] + [O] = CrO(s)	−236,320	113.6
2[Cr] + [N] = Cr_2N(s)	−141,300	116.82
[Cr] + [N] = CrN(s)	−136,250	96.2
[Ni] + [O] = NiO(s)	−125,000	136.29

Table 1. The possible reactions and standard Gibbs free energy in liquid.

Reaction equations in solid phase(γ)	$\Delta G^{\theta} = A + B \times T$, J·mol^{-1}	
	A	***B***
[Al] + [N] = AlN(s)	−137536.1	34.27
[Mn] + [S] = MnS(s)	−176,782	57.91
[Ti] + [N] = TiN(s)	−153158.23	6.13
[Ti] + [C] = TiC(s)	−143585.84	52.65
[Nb] + [N] = NbN(s)	−162730.62	53.6
[Nb] + [C] = NbC(s)	−143585.84	56.67
[V] + [N] = VN(s)	−182030.1	207.39
[V] + [C] = VC(s)	−797,190	349.72

Table 2. The possible reactions and standard Gibbs free energy in solid.

$$SiO_2(s) = SiO_2(l) \quad \Delta G^{\theta} = 9581.3 - 4.8T \quad J \cdot mol^{-1} \tag{7}$$

$$xCe_2O_3(l) + yAl_2O_3(l) + (1 - x - y)SiO_2(l) = Ce_{2x}Al_{2y}Si_{1-x-y}O_z(l) \tag{8}$$

where the standard Gibbs free energy of reactions 2, 3, 4 are listed in **Table 1**. And the CALPHD technique was used to optimize the Gibbs free energy change of reaction 8. The Redlich-Kister (R-K) expression was adopted to describe the excess Gibbs free energy of solution phases in Al_2O_3-SiO_2, Al_2O_3-Ce_2O_3 and Ce_2O_3-SiO_2 binary systems. The R-K expression is written as Eq. 9.

$$\begin{aligned} G^E &= x_1 x_2 \sum_{j=0}^{n} L_j (x_1 - x_2)^j \\ &= x_1 x_2 L_0 \\ &+ x_1 x_2 L_1 (x_1 - x_2) \\ &+ x_1 x_2 L_2 (x_1 - x_2)^2 \\ &+ \cdots \end{aligned} \tag{9}$$

where G^E is the excess Gibbs free energy of binary system; x_1, x_2 are the mole fraction of end members in the binary system; L_j (j = 0, 1, 2…) are the interaction parameters of components in the binary system. And L_j in **Table 3** were obtained by the phase diagram optimization when the restricted experimental points from literature were employed.

The excess Gibbs free energy of Ce_2O_3-Al_2O_3-SiO_2 ternary system was derived by the following geometric Kohler method [38].

$L_i = a + bT/(\mathrm{J\cdot mol^{-1}})$		L_0	L_1	L_2	L_3
Al_2O_3-SiO_2	*a*	19570.28	14875.48	5640.02	—
	b	−10.49	−0.71	1.21	—
Ce_2O_3-Al_2O_3	*a*	−78839.95	—	—	—
	b	−30.23	—	—	—
Ce_2O_3-SiO_2	*a*	−140979.96	215301.91	547791.07	398115.65
	b	78.91	23.60	−202.71	−155.94

Table 3. The optimized coefficients of the binary systems.

$$\begin{aligned} G^{\mathrm{E}}_{extra} &= (x_1+x_2)^2 G^E_{12}\left(\frac{x_1}{x_1+x_2},\frac{x_2}{x_1+x_2}\right) \\ &+(x_2+x_3)^2 G^E_{23}\left(\frac{x_2}{x_2+x_3},\frac{x_3}{x_2+x_3}\right) \\ &+(x_1+x_3)^2 G^E_{13}\left(\frac{x_1}{x_1+x_3},\frac{x_3}{x_1+x_3}\right) \end{aligned} \tag{10}$$

where the first term $G^E_{12}\left(\frac{x_1}{x_1+x_2},\frac{x_2}{x_1+x_2}\right)$ is the excess Gibbs free energy at $\left(\frac{x_1}{x_1+x_2},\frac{x_2}{x_1+x_2}\right)$ point in the 1–2 binary system. The following two terms in Eq. 10 have similar representation as the first term. In order to exactly describe the thermodynamic properties of Ce_2O_3-Al_2O_3-SiO_2 system, the Gibbs free energy was further modified by the $G^E_{ternary}$ term with the value of -825000$x_{Ce_2O_3}$ $x_{Al_2O_3}x^2_{SiO_2}$. After the interaction coefficients in **Table 3** are imported, the standard Gibbs free energy of reaction 8 is written as:

$$\begin{aligned} \Delta G^{\theta}_{\mathrm{L}} &= G^{idea}+G^E = G^{idea}+G^E_{extra}+G^E_{ternary} \\ &= -825000xy(1-x-y)^2+42569.73xy+19570.28y(1-y)-140979.96x(1-x) \\ &+\frac{y(1-x-y)(1-x-2y)}{1-x}\left(14875.48+5640.02\frac{1-x-2y}{1-x}\right) \\ &+\frac{x(1-x-y)(1-2x-y)}{1-y}\left[215301.91+547791.07\frac{1-2x-y}{1-y}+398115.65\left(\frac{1-2x-y}{1-y}\right)^2\right] \\ &+\left\{\begin{array}{l} -98.65xy-10.49y(1-y)+78.91x(1-x) \\ +\frac{y(1-x-y)(1-x-2y)}{1-x}\left[-0.71+1.21\frac{1-x-2y}{1-x}\right] \\ +\frac{x(1-x-y)(1-2x-y)}{1-y}\left[23.6-202.71\frac{1-2x-y}{1-y}-155.94\left(\frac{1-2x-y}{1-y}\right)^2\right] \\ +8.314[x\ln x+y\ln y+(1-x-y)\ln(1-x-y)] \end{array}\right\}T \end{aligned} \tag{11}$$

When the Gibbs free energy of Eqs. (2)–(8) are introduced, the standard Gibbs free energy of Eq. (1) is finally written as follows:

$$\begin{aligned}\Delta G_{\mathrm{L}}^{\theta} &= -825000xy(1-x-y)^2 + 42569.73xy + 19570.28y(1-y) - 140979.96x(1-x)\\ &- 1368003.6x - 1094333.3y - 570968.7(1-x-y)\\ &+ \frac{y(1-x-y)(1-x-2y)}{1-x}\left(14875.48 + 5640.02\frac{1-x-2y}{1-x}\right)\\ &+ \frac{x(1-x-y)(1-2x-y)}{1-y}\left[215301.91 + 547791.07\frac{1-2x-y}{1-y} + 398115.65\left(\frac{1-2x-y}{1-y}\right)^2\right]\\ &+ \left\{\begin{array}{l} -98.65xy - 10.49y(1-y) + 78.91x(1-x) + 334.96x + 340.92y + 216.23(1-x-y)\\ +\frac{y(1-x-y)(1-x-2y)}{1-x}\left[-0.71 + 1.21\frac{1-x-2y}{1-x}\right]\\ +\frac{x(1-x-y)(1-2x-y)}{1-y}\left[23.6 - 202.71\frac{1-2x-y}{1-y} - 155.94\left(\frac{1-2x-y}{1-y}\right)^2\right]\\ +8.314[x\ln x + y\ln y + (1-x-y)\ln(1-x-y)]\end{array}\right\}T\end{aligned} \tag{12}$$

After the standard Gibbs free energy $\Delta G_{\mathrm{L}}^{\theta}$ of liquid inclusions formation was worked out, the inclusions compositions (certain x, y values, $z = 1-x-y$) can be calculated according to the minimum of Gibbs free energy ΔG_{L}. At the equilibrium status in the molten steel, the Gibbs free energies of chemical reactions in **Table 1** are greater than or equal to zero.

3. Modeling validation

The constructed model was validated by plant trial, lab scale experiments and experimental data from others work. Moreover, the calculated results by this model were compared with the popular commercial software FactSage.

The standard chemical compositions of 253MA steel were shown in **Table 4**. And the industrial samples of 253MA steel were obtained after EAF → AOD → LF → CC process in one stainless steel plant of China. The obtained samples were machined into column of $\Phi = 4$ mm

C	Si	Mn	S	P	N	Ni	Cr	Ce
0.05–0.10	1.40–2.0	≤0.80	≤0.030	≤0.040	0.14–0.20	10.00–12.00	20.00–22.00	0.03–0.08

Table 4. The chemical compositions of 253MA steel (mass fraction, %).

and then polished by emery paper and polishing cloth to make metallographic specimen. Then the field emission scanning electron microscope (FE-SEM) and energy dispersive spectrometer (EDS) were employed to observe the morphology and analyze the compositions of inclusions, as shown in **Figure 2**. It can be seen that the inclusions with the size of 1-2 μm in the solidification structure of 253 MA steel are mainly Ce_2O_2S and Ce_2O_3. CeN maybe exist as the element N was detected as shown in **Figure 2(b)**. The peaks without labels are matrix elements Fe, Cr and Ni.

The experiments in laboratory that carefully follows the industrial operations were carried out in the Si-Mo rod heating furnace protected by argon flow at 1873 K, as shown in **Figure 3**. Firstly, the Fe-Cr-Ni alloys with fixed ratio as in the 253MA steel were loaded in the MgO crucible until completely melted. Then the mass fraction of Si was calculated and added into the crucible after the oxygen content was first determined. After Si was totally melted, the oxygen content was determined for the second time and then the melt was alloyed by Ce. The molten steel was drawn using quartz tube (inner Φ = 4 mm) and immediately quenched into ice water at 30 min after Ce addition. Therefore, the inclusions formed at 1873 K can be preserved since the extremely cooling rate of quenching. The quenched samples were processed and observed as the same as that of industrial samples. It is explicit that the inclusions are Ce_2O_2S and Ce_2O_3 with the size smaller than 2 μm as the analysis results shown in **Figure 4**.

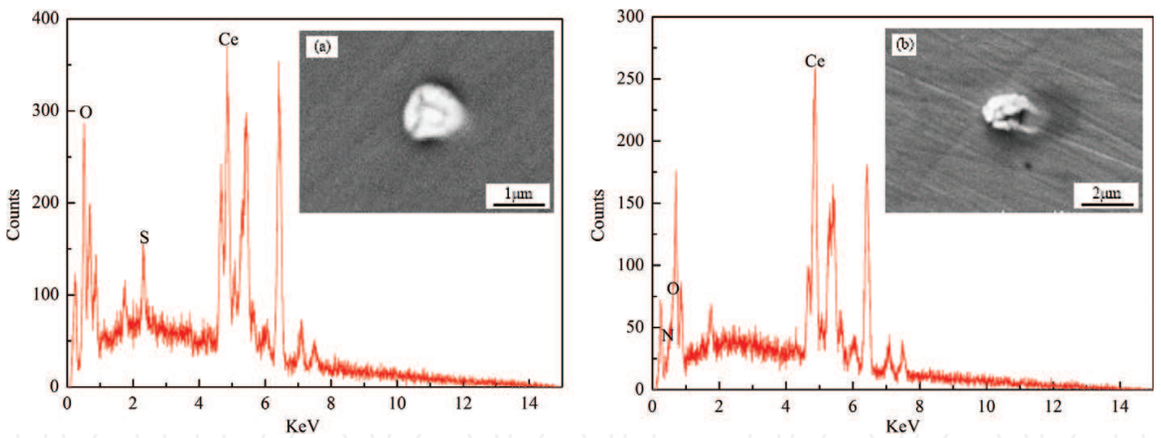

Figure 2. SEM images and EDS analysis of inclusions in the solidification structure.

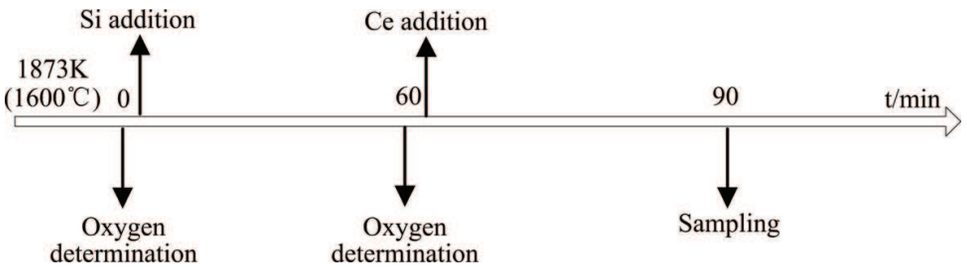

Figure 3. The flow chart of technological process of lab scale experiment.

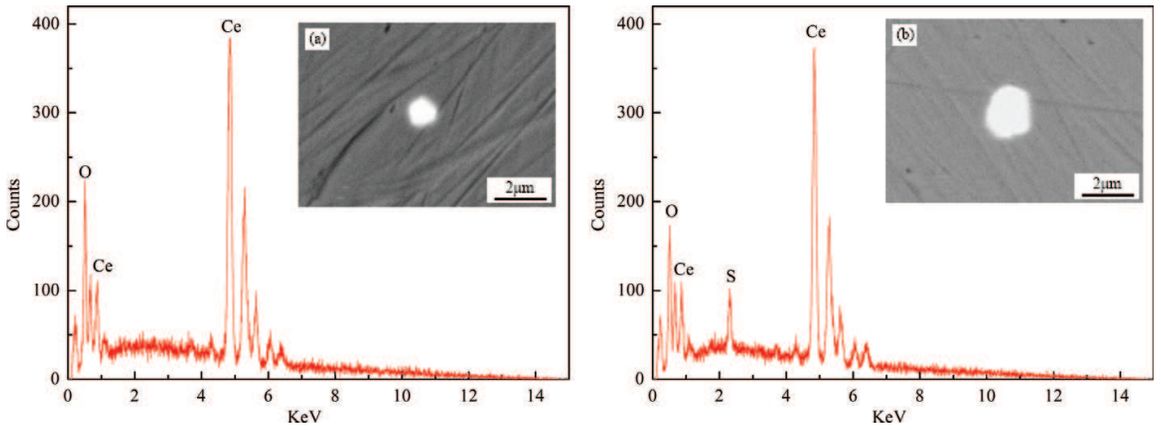

Figure 4. SEM images and EDS analysis of inclusions in the laboratory sample.

The types and amounts of inclusions formed during the solidification of 253MA steel was calculated by the present model and the results are drawn in **Figure 5** which (b) is the zoom view of the liquid–solid two-phase region (T_L = 1713 K). It can be seen that the inclusions types are mainly Ce_2O_2S, Ce_2O_3, CeN and Ce_2SiO_5. And the calculation results are in agreement with the industrial experiments except Ce_2SiO_5. Ce_2SiO_5 is formed as Ce_2O_3 is reduced during solidification as shown in the magnified image of **Figure 5(b)**. Then Ce_2SiO_5 must be transformed from Ce_2O_3 as the increasing Si concentration in the residual liquid phase which owes to the micro-segregation of solutes at the liquid–solid interface. However, it is very difficult for the decomposition of Ce_2O_3 because the extremely fast cooling rate during the continuous casting process. Therefore, Ce_2SiO_5 is not found in the industrial samples. What is more, the formed inclusions are only Ce_2O_3 and Ce_2O_2S at 1873 K which is completely consistent with the results in the laboratory scale experiments.

The types and amounts of inclusions formed during the solidification of 253MA steel was also calculated by FactSage and the results are drawn in **Figure 6**. It can be seen that only Ce_2O_3 and Ce_2O_2S are formed in the FactSage results where Ce_2O_2S precipitates at a lower temperature 1848 K comparing with 1873 K in the present model. However, Ce_2SiO_5 and CeN are not present in the FactSage results since the solutes segregation is not considered in FactSage when

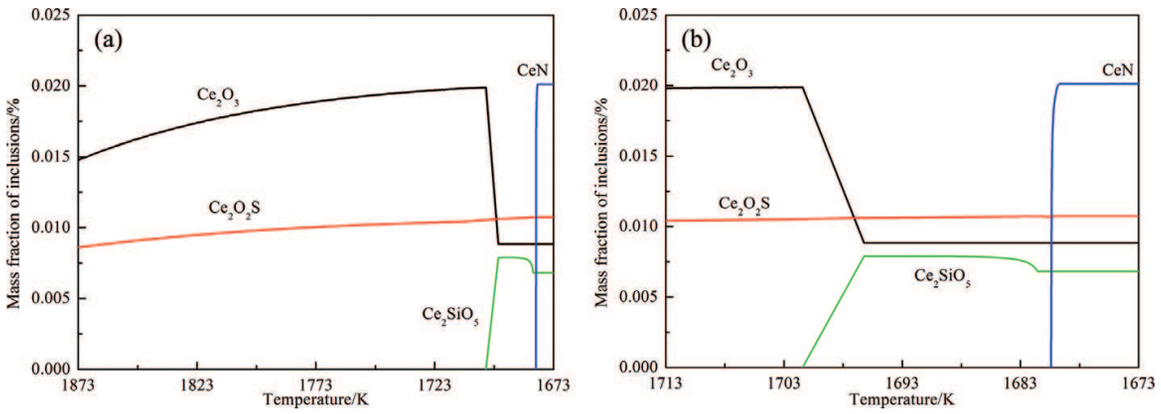

Figure 5. The precipitation behavior of inclusions during solidification of 253MA steel.

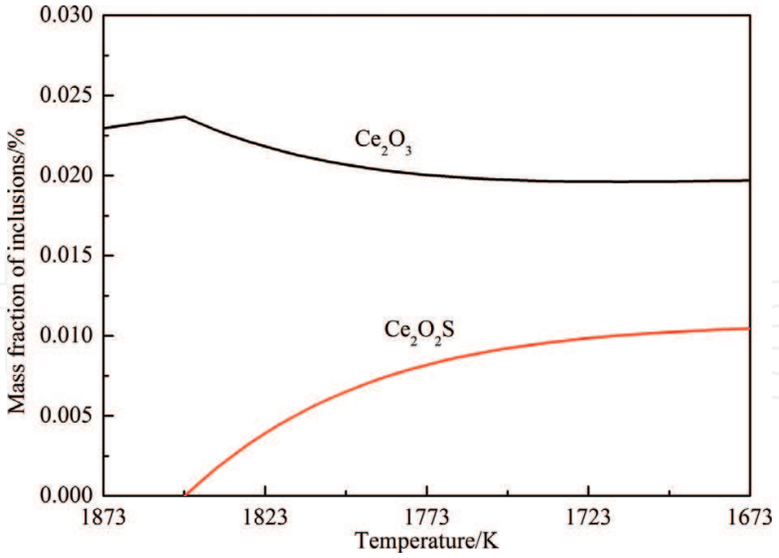

Figure 6. The precipitation behavior of inclusions calculated by FactSage.

the normal equilibrium solidification model is selected. The elements activities were further calculated to understand the lower formation temperature of Ce_2O_2S in FactSage. The stable pure substances at standard conditions are adopted by FactSage as the activities standard sate when 1mass% infinite dilute solution is chosen in the present work. The activities of solutes in molten steel calculated by the two different standard states can be linked by the following equation.

$$a_{i(w)}^{\mathrm{H}} = \frac{100M_i}{M_{\mathrm{A}}\gamma_i^0} * a_i^{\mathrm{R}} \tag{13}$$

where $a_{i(w)}^{\mathrm{H}}$ is the activity at the standard state of 1 mass% solution; a_i^{R} is the activity when pure substance is standard state; M_i is the relative atomic mass of solutes; M_{A} is the relative atomic mass of solvents, that is Fe in this work; γ_i^0 is the activity coefficient when stable pure substance is standard state in the Henrian solution. The available activity coefficients are listed in **Table 5** [39] and the activities transformed from FactSage state to 1 mass% solution comparing with that calculated by this model are present in **Table 6**.

As listed in **Table 6**, the solutes activities calculated from different standard state are basically at the same level except P and N elements. The remarkable differences of P and N activities can

	C	Si	Mn	Ce	O
A	$e^{0.57}$	−11763.2	0	−7103.2	−15,280
B		0		0	3.5
Standard state	S	S	L	L	G

Note: $\ln\gamma^0 = A/T + B$, *e*: natural constant, S: pure solid, L: pure liquid, G: gas.

Table 5. Optimized Henrian activity coefficients $\ln\gamma^0$.

	C	Si	Mn	P	S	N	Ce	O
This work	4.23E-2	3.10	5.74E-1	2.78E-2	7.15E-4	1.50E-2	2.09E-3	2.82E-4
FactSage	3.08E-2	2.64	5.20E-1	9.30E-5	1.39E-4	13.2	1.24E-3	1.86E-4

Table 6. The activities calculated by this work and FactSage at 1873 K.

Authors	RE addition/%	Inclusions found	Predicted by this model
Yue [40]	0.016	Rare earth sulfides	Ce_2S_3
Liu [41]	0.044	Rare earth oxysulfides	Ce_2O_2S, CeS
Guo [42]	0.034	Ce_2O_2S, CeS	Ce_2O_2S, Ce_2O_3, CeN
Zhai [43]	0.08	Ce_2O_2S, Ce_2O_3, CeO_2	Ce_2O_2S, Ce_2O_3
Factsage	0.04	Ce_2O_3, Ce_2O_2S	Ce_2O_3, Ce_2O_2S, Ce_2SiO_5, CeN
Present work	0.04	Ce_2O_3, Ce_2O_2S, CeN	Ce_2O_3, Ce_2O_2S, Ce_2SiO_5, CeN

Table 7. Comparison of inclusions from literature experiments and predicted by this work.

owe to the missing γ_i^0 values of P and N. It can be seen that the sulfur activity calculated by FactSage is smaller than that calculated by this model because γ_i^0 of S is not available. It is the direct explanation why the formation temperature of Ce_2O_2S is lower in the FactSage results.

Besides the industrial trials and lab scale experiments, the types of inclusions reported in the steel containing rare earth elements from literature were compared with the model prediction and the results are present in **Table 7**. The types of generated inclusions in various grades of steels reported in others work are almost the same as the results calculated by this model.

All the above comparisons send the message that the accomplished coupled thermodynamic in this work is precise and it is competent to exactly assess the precipitation behaviors of inclusions during solidification process of various grades of steels containing rare earth elements.

4. Model application

Aluminum was alloyed in the heat-resistant steel imitating the calcium treatment way to solve the nozzle clogging of 253MA steel. Since the formed inclusions resulting in nozzle clogging are mainly oxides, the inclusions transformation at different initial oxygen contents was studied. And the types of inclusions formed before and after aluminum addition are shown in **Figure 7**. It can be seen that the stable inclusion at high oxygen content is $Ce_2Si_2O_7$ in steel without aluminum. By contrast, the inclusions eventually transform to liquid phase as oxygen content increases to 0.018% after 0.01mass% aluminum was added in 253MA steel.

In addition, the stable areas of inclusions (predominance area diagram of inclusions or phase diagram of inclusions) in heat-resistant steel at 1873 K are summarized in **Figure 8**. The stable

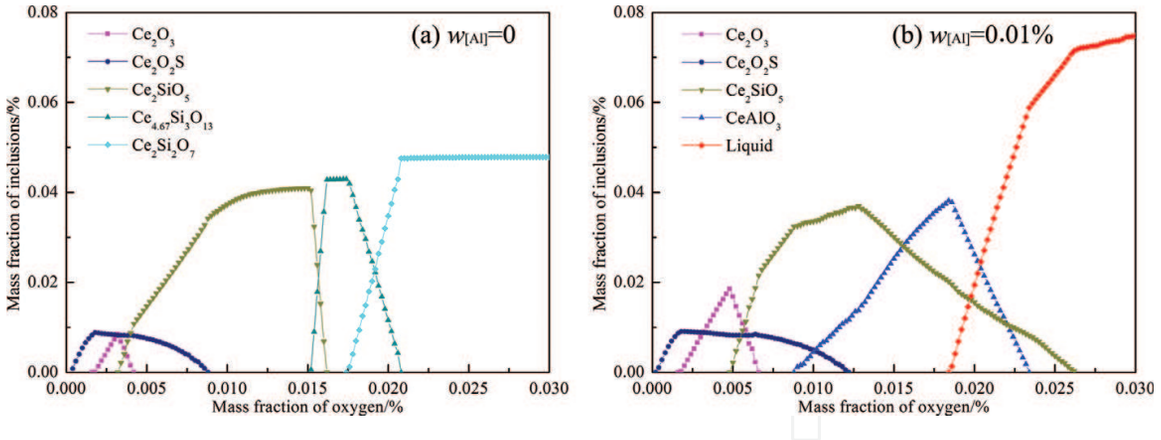

Figure 7. The inclusions types in heat-resistant steel at 1873 K.

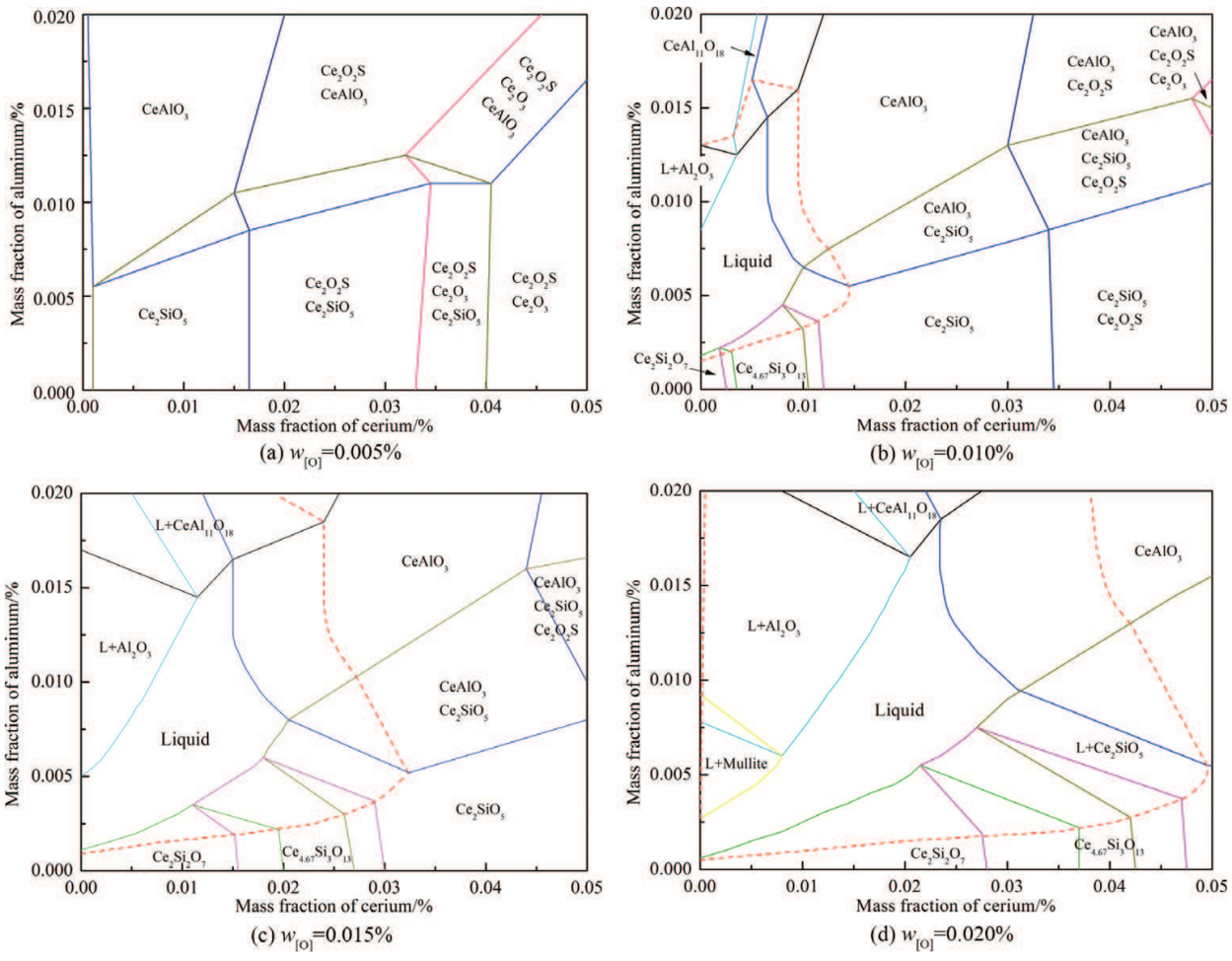

Figure 8. The stability areas of inclusions at 1873 K.

regions of liquid inclusions are surrounded by the dash line. There is not liquid inclusions formed when the oxygen content is low (0.005% in this study). And the stable areas of liquid inclusions are growing as the increasing initial oxygen content. There can be no doubt that

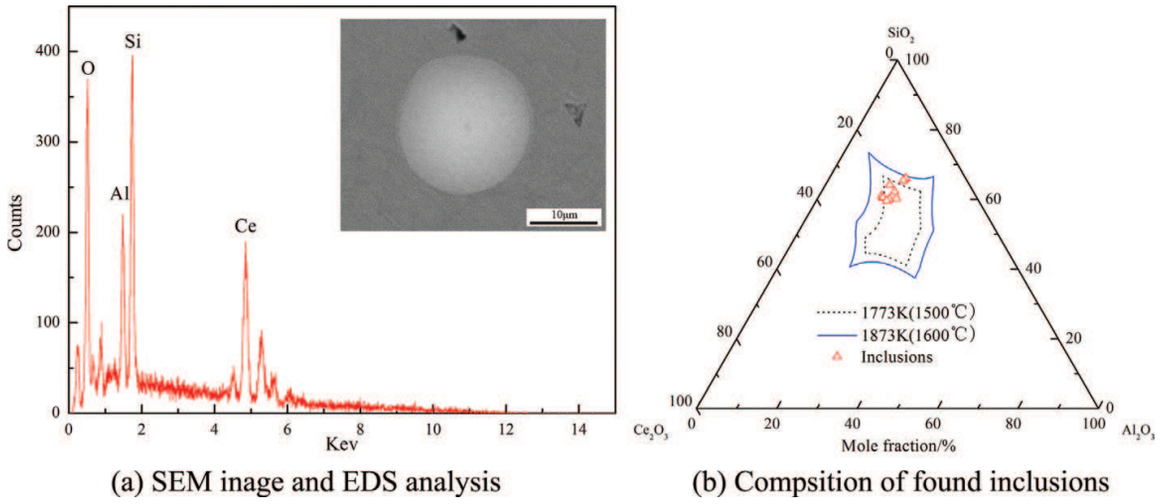

Figure 9. The liquid inclusions in heat-resistant.

stable areas of liquid phase will be helpful to solve the nozzle clogging issue of steels alloyed by rare earth elements.

In 2011, Kojola [6] reported that the clogging rate of 253MA steel dramatically decreased when Al, Si and Ce co-existed in the molten steel. Kojola argued that the small rare earth oxides can be dissolved after Si addition because of the negative interaction of Si to oxygen. However, no convincing proof was given. It is clear that the liquid inclusions are formed according to the prediction by the model in this work. Moreover, based on the calculated stable areas of inclusions the lab scale experiments following the procedure in **Figure 3** were carried out when Si-Al alloy was chosen instead of pure Si. The FE-SEM image and EDS analysis of found inclusions were shown in **Figure 9(a)**. The inclusions were complex phases of Ce-Al-Si-O system with the large size of 15 μm. And the complex inclusions were in the liquid region at 1873 K when be marked in the Al_2O_3-SiO_2-Ce_2O_3 phase diagram.

5. Conclusions

A coupling model of inclusions generation and solutes micro-segregation during the solidification process of steels containing rare earth elements was worked out. The method for calculating the Gibbs free energy of liquid inclusions was first given. Then the reliability of mathematical model was validated by the industrial sampling, experiments in lab scale and inclusions found in literature. The inclusions calculated by FactSage software were different from this model because of the differences in the activity standard state and the solidification model. The inclusions are Ce_2O_3, Ce_2O_2S and CeN in the solidification structure of 253MA steel. These small size inclusions containing rare earth elements can be modified to the liquid inclusions after Al adding and the stable liquid regions increase as the initial oxygen content increases. Moreover, the complex liquid inclusions of Ce-Al-Si-O system were found in the preliminary experiments of lab scale. The coupling model is helpful to relieve the nozzle clogging issue of various grades of steel containing rare earth elements.

Acknowledgements

This work was supported by the Scientific Research Foundation for Scholars in Yangtze Normal University No. 2016KYQD14, No. 2016XJQN34.

Author details

Yandong Li[1]*, Huamei Duan[2] and Cheng Peng[1]

*Address all correspondence to: andyydlee@gmail.com

1 Key Laboratory of Extraordinary Bond Engineering and Materials, Yangtze Normal University, Chongqing, China

2 College of Materials Science and Engineering, Chongqing University, Chongqing, China

References

[1] Chen L, Ma XC, Wang LM, Ye XN. Effect of rare earth element yttrium addition on microstructures and properties of a 21Cr-11Ni austenitic heat-resistant stainless steel. Materials and Design. 2011;**32**(4):2206-2212. DOI: 10.1016/j.matdes.2010.11.022

[2] Matway RJ, McGuire MF, Mehta J. Steel alloy having improved creep strength. US. Patent. 1995

[3] Nilsson JO. The influence of nitrogen on high temperature low cycle fatigue behaviour of austenitic stainless steels. Fatigue & Fracture of Engineering Materials & Structures. 1987;**7**(1):55-64. DOI: 10.1111/j.1460-2695.1984.tb00359.x

[4] Cai GJ, Li CS. Effects of Ce on inclusions and corrosion resistance of low-nickel austenite stainless steel. Materials and Corrosion. 2015;**66**(12):1445-1455. DOI: 10.1002/maco.201508380

[5] Waudby PE. Rare earth additions to steel. International Metals Reviews. 1978;**23**(1):74-98. DOI: 10.1179/imtr.1978.23.1.74

[6] Kojola N, Ekerot S, Andersson M, Jönsson P. Pilot plant study of nozzle clogging mechanisms during casting of REM treated stainless steels. Ironmaking and Steelmaking. 2011;**38**(1):1-11. DOI: 10.1179/030192310X12690127076398

[7] Kojola N, Ekerot S. Pilot plant study of clogging rates in low carbon and stainless steel grades. Ironmaking & Steelmaking. 2011;**38**(2):81-89. DOI: 10.1179/030192310X12706364542704

[8] Roos E, Karasev A, Jönsson PG. Effect of Si and Ce contents on the nozzle clogging in a REM alloyed stainless steel. Steel Research International. 2015;**86**(11):1279-1288. DOI: 10.1002/srin.201400344

[9] Yao YK, Zhu MW, Wang DY, Liu CJ, Jiang MF. Investigation of nozzle blockage mechanism during feeding RE into tundish. Chinese Eare Earth. 2004;**25**(5):17-19. DOI: 10.16533/j.cnki.15-1099/tf.2004.05.006

[10] Lind M, Holappa L. Transformation of alumina inclusions by calcium treatment. Metallurgical and Materials Transactions B. 2010;**41**(2):359-366. DOI: 10.1007/s11663-009-9337-9

[11] Janke D, Ma Z, Valentin P, Heinen A. Improvement of castability and quality of continuously cast steel. ISIJ International. 2000;**40**(1):31-39. DOI: 10.2355/isijinternational.40.31

[12] Holappa L, Hämäläinen M, Liukkonen M, Lind M. Thermodynamic examination of inclusion modification and precipitation from calcium treatment to solidified steel. Ironmaking & Steelmaking. 2003;**30**(2):111-115. DOI: 10.1179/030192303225001748

[13] Yang J, Wang XH, Jiang M, Wang WJ. Effect of calcium treatment on non-metallic inclusions in ultra-low oxygen steel refined by high basicity high Al_2O_3 slag. Journal of Iron and Steel Research, International. 2011;**18**(7):8-14. DOI: 10.1016/S1006-706X(11)60083-6

[14] Zhang LF, Ren Y, Duan HJ, Yang W, Sun LY. Stability diagram of Mg-Al-O system inclusions in molten steel. Metallurgical and Materials Transactions B. 2015;**46**(4):1809-1825. DOI: 10.1007/s11663-015-0361-7

[15] Zhang TS, Min Y, Jiang MF. Effect of magnesium addition on evolution of inclusions in Mn–Si–Al deoxidised molten steels. Canadian Metallurgical Quarterly. 2015;**54**(2):161-169. DOI: 10.1179/1879139514Y.0000000173

[16] Fujii K, Nagasaka T, Hino M. Activities of the constituents in spinel solid solution and free energies of formation of MgO, $MgO{\cdot}Al_2O_3$. ISIJ International. 2000;**40**(11):1059-1066. DOI: 10.2355/isijinternational.40.1059

[17] Park JH, Todoroki H. Control of MgO Al_2O_3 spinel inclusions in stainless steels. ISIJ International. 2010;**50**(10):1333-1346. DOI: 10.2355/isijinternational.50.1333

[18] Ren Y, Zhang LF, Yang W, Duan HJ. Formation and thermodynamics of Mg-Al-Ti-O complex inclusions in Mg-Al-Ti-deoxidized steel. Metallurgical and Materials Transactions B. 2014;**45**(6):2057-2071. DOI: 10.1007/s11663-014-0121-0

[19] Zhang TS, Min Y, Liu CJ, Jiang MF. Effect of Mg addition on the evolution of inclusions in Al–Ca deoxidized melts. ISIJ International. 2015;**55**(8):1541-1548. DOI: 10.2355/isijinternational.ISIJINT-2014-691

[20] Harada A, Maruoka N, Shibata H, Kitamura S. A kinetic model to predict the compositions of metal, slag and inclusions during ladle refining: Part 1. Basic concept and application. ISIJ International. 2013;**53**(12):2110-2117. DOI: 10.2355/isijinternational.53.2110

[21] Harada A, Maruoka N, Shibata H, Kitamura S. A kinetic model to predict the compositions of metal, slag and inclusions during ladle refining: Part2. Condition to control the inclusion composition. ISIJ International. 2013;**53**(12):2118-2125. DOI: 10.2355/isijinternational.53.2118

[22] Liu ZZ, Wei J, Cai KK. A coupled mathematical model of microsegregation and inclusion precipitation during solidification of silicon steel. ISIJ International. 2002;**42**(9):958-963. DOI: 10.2355/isijinternational.42.958

[23] Fang L, Liu HL, Liu CJ, Jiang MF. Model analysis on behavior of cerium in heavy rail steel. Chinese Rare Earth. 2008;**29**(1):88-91. DOI: 10.3969/j.issn.1004-0277.2008.01.022

[24] Li YD, Liu CJ, Li CL, Jiang MF. A coupled thermodynamic model for prediction of inclusions precipitation during solidification of heat-resistant steel containing cerium. Journal of Iron and Steel Research, International. 2015;**22**(6):457-463. DOI: 10.1016/S1006-706X(15)30027-3

[25] Clyne TW, Kurz W. Solute redistribution during solidification with rapid solid state diffusion. Metallurgical and Materials Transactions A. 1981;**12**(6):965-971. DOI: 10.1007/BF02643477

[26] Vahed A, Kay DAR. Thermodynamics of rare earths in steelmaking. Metallurgical Transactions B. 1976;**7**(3):375-383. DOI: 10.1007/BF02652708

[27] Turkdogan ET. Physical Chemistry of High Temperature Technology. New York: Academic Press; 1980

[28] Alaoua D, Lartigue S, Larere A, Priester L. Precipitation and surface segregation in low carbon steels. Materials Science and Engineering A. 1994;**189**(1–2):155-163. DOI: 10.1016/0921-5093(94)90411-1

[29] Yamamoto K, Hasegawa T, Takamura JI. Effect of boron on intra-granular ferrite formation in Ti-oxide bearing steels. ISIJ International. 1996;**36**(1):80-86. DOI: 10.2355/isijinternational.36.80

[30] Taylor KA. Solubility products for titanium-, vanadium-, and niobium-carbide in ferrite. Scripta Metallurgica et Materialia. 1995;**32**(1):7-12

[31] ParK JY, Park JK, Choo WY. Effect of Ti addition on the potency of MnS for ferrite nucleation in C–Mn–V steels. ISIJ International. 2000;**40**(12):1253-1259. DOI: 10.2355/isijinternational.40.1253

[32] Chen EB, Dong YC, Guo SZ. Study on thermodynamical properties in Mn-Fe alloy melts. Acta Metallgugica Sinica. 1997;**33**(8):831-837

[33] Du T. Themodynamics of rare earth elements in iron-base solutions. Journal of Iron and Steel Research. 1994;**6**(3):6-12. DOI: 10.13228/j.boyuan.issn1001-0963.1994.03.002

[34] Yue EB, Qiu ST, Gan Y. Carbo-nitride precipitation model in austenite of HSLA steel. Journal of Iron and Steel Research. 2006;**18**(8):49-52. DOI: 10.3321/j.issn:1001-0963.2006.08.012

[35] Tang GB, Wu XY, Yong X, Bai AM, Liu ZD, Yong QL. Numerical simulation of thermodynamic for carbonitride precipitationin austenite of complex microalloyed high strength and low alloy steels. Heat Treatment Metals. 2008;**33**(8):67-72. DOI: 10.13251/j.issn.0254-6051.2008.08.044

[36] Luo S, Zhu MY, Ji C, Cai ZZ. Solute microsegregation model for continunous casting process of steel. Iron and Steel. 2010;**45**(6):31-36

[37] Zhang MC, Li SZ, Zhang QY, Zhang JP. Thermodynamic study on carbide and nitride precipitation of X60 pipeline steel in continuous casting. Journal of Anhui University of Technology (Natural Science). 2012;**29**(3):207-210. DOI: 10.3969/j.issn.1671-7872.2012.03.004

[38] Pelton AD. A general "geometric" thermodynamic model for multicomponent solutions. Calphad. 2001;**25**(2):319-328. DOI: 10.1016/S0364-5916(01)00052-9

[39] Jung IH, Decterov SA, Pelton AD. A thermodynamic model for deoxidation equilibria in steel. Metallurgical and Materials Transactions B. 2004;**35**(3):493-507. DOI: 10.1007/s11663-004-0050-4

[40] Yue LJ, Wang LM, Han JS. Effects of rare earth on inclusions and corrosion resistance of 10PCuRE weathering steel. Journal of Rare Earths. 2010;**28**(6):952-956. DOI: 10.1016/S1002-0721(09)60219-2

[41] Liu X, Yang JC, Gao XZ. Effects of RE on the inclusions and impact toughness of 2Cr13 stainless steel. Journal of University of Science and Technology Beijing. 2010;**32**(5):605-609

[42] Guo F, Lin Q, Sun XX. Thermodynamic calculation on precipitation and transformation of inclusions in high purity carbon-manganese steels with rare earths and their microstructure analysis. Journal of the Chinese Rare Earth Society. 2004;**22**(5):624-618. DOI: 10.3321/j.issn:1000-4343.2004.05.006

[43] Zhai QJ. Study on microstructure and formation mechanism of rare earth inclusions during solidification (Chinese edition). Journal of the Chinese Rare Earth Society. 1995;**13**(1):60-62

IntechOpen